

# An infrared, Raman, and X-ray database of battery interphase components

Lukas Karapin-Springorum<sup>1,2</sup>, Asia Sarycheva<sup>1</sup>, Andrew Dopilka<sup>1</sup>, Hyungyeon Cha<sup>1</sup>,  
Muhammad Ihsan-UI-Haq<sup>1</sup>, Jonathan M. Larson<sup>1,3\*</sup>, and Robert Kostecki<sup>1\*</sup>

1. Energy Storage & Distributed Resources Division, Lawrence Berkeley National Laboratory, Berkeley, California, 94720, USA
2. Department of Physics and Astronomy, Pomona College, Claremont, California, 91711, USA (Current Address)
3. Department of Chemistry and Biochemistry, Baylor University, Waco, Texas, 76798, USA (Current Address)

*\*These authors jointly supervised this work*

corresponding authors: Robert Kostecki ([R\\_Kostecki@lbl.gov](mailto:R_Kostecki@lbl.gov)), Jonathan M. Larson ([Jonathan\\_Larson@Baylor.edu](mailto:Jonathan_Larson@Baylor.edu))

## Abstract

Further technological advancement of both lithium-ion and emerging battery technologies can be catalyzed by an improved understanding of the chemistry and working mechanisms of the solid electrolyte interphases (SEIs) that form at electrochemically active battery interfaces. However, collecting and interpreting spectroscopy results of SEIs is difficult for several reasons, including the chemically diverse composition of SEIs. To address this challenge, we herein present a vibrational spectroscopy and X-ray diffraction data library of ten suggested SEI chemical constituents relevant to both lithium-ion and emerging battery chemistries. The data library includes attenuated total reflectance Fourier transform infrared spectroscopy, Raman spectroscopy, and X-ray diffraction data, collected in inert atmospheres afforded by custom designed sample holders. The data library presented in this work (and online repository) alleviates challenges with locating related work that is either diffusely spread throughout the literature, or is non-existent, and provides energy storage researchers streamlined access to vital SEI-relevant data that can catalyze future battery research efforts.

## Background & Summary

Energy storage technologies play a large and growing role in humans' lives and will continue to do so for the foreseeable future. Currently, for many applications, rechargeable lithium-ion batteries (LIBs) have requisite energy and power densities as well as adequate cycle and calendar life at reasonable cost relative to other energy storage technologies.<sup>1,2</sup> As a result, LIBs (with various cathode materials) are used extensively in consumer electronics,<sup>3</sup> deployed in electric vehicles,<sup>4</sup> and are beginning to be used in the electric grid to store energy from intermittent renewable sources.<sup>1,5,6</sup> That said, there is still need for a number of innovations to increase safety and recyclability, reduce cost, and optimize the performance of LIBs to enable additional applications (e.g. aviation, long duration storage) while using materials that minimize supply chain and ethical mining concerns.

From a basic science perspective, many key performance characteristics of LIBs are enabled by the natural formation of solid electrolyte interphases (SEIs) at electrochemically active interfaces. This is because SEIs regulate mass and charge transfer across the interface, as well as the degree of passivation at the interface.<sup>7</sup> A critically important SEI in modern LIBs is the SEI that forms at the interface between the electrolyte and graphite anode, which conducts lithium ions – enabling ion intercalation and deintercalation during charging and discharging – but is an electrical insulator, mitigating deleterious side reactions.<sup>8-10</sup> Fortuitously, the anodic SEI grown during initial formation cycling is quite stable.<sup>11</sup>

It is widely believed that the performance and lifetime of state-of-the-art LIBs and next-generation variants (e.g. those that utilize novel electrochemical intercalation chemistries or the conversion or plating of lithium) can be substantially improved through targeted engineering efforts informed by an improved understanding of the basic structure, chemistry, and working mechanisms of the SEI.<sup>12-15</sup> However, it is difficult to develop an understanding of fundamental structure-function relationships in SEIs in part because they are reactive, chemically heterogeneous, difficult to isolate and sense (being extremely thin, on the order of tens of nanometers thick), and because they are buried between dissimilar materials.<sup>13</sup> Further, the composition of SEIs can depend on manufacturing procedures, cycling conditions, and other physical circumstances which are not always standardized.<sup>8,10,13</sup>

Fourier transform infrared spectroscopy (FTIR) and Raman spectroscopy are commonly used to characterize SEI chemistry and structure, while X-ray diffraction (XRD) can characterize SEI crystallinity, which influences ionic conductivity.<sup>10,13</sup> However, it is often difficult to interpret the data generated by these techniques because of a large mix of contributions to the data, including those from numerous chemical components of the SEI, as well as from other parts of the electrochemical cell (like active electrode materials and current collectors). By various estimates, the SEI has more than ten unique chemical constituents.<sup>13,16</sup> As a result, reference measurements of individual candidate compounds are often used to identify the multiple chemicals contributing to complex spectra. Although some spectral databases exist to assist in this,<sup>17,18</sup> access to these can be prohibitively expensive, or lack needed data. Furthermore, researchers can, of course, collect reference spectra themselves or look to the literature. However, the former is time consuming and possibly costly, and the latter can be challenging for the following reasons. First, published measurements of oxygen- and water-reactive compounds may include varying degrees of contribution from unwanted reaction products that may obscure features of interest. Second, the desired data is commonly difficult to find, being included in articles unrelated to SEI characterization, published in supplemental information sections, or plotted along other data. Finally, if appropriate data is found in the literature, it is not usually offered in a digitized form for streamlined use.

In order to reduce these practical challenges faced by energy storage researchers in the identification of SEI constituents, we present this work, with corresponding online data library posted on Dryad, of measurements of pristine and unreacted SEI components relevant to current and emerging LIB technologies, using attenuated total reflectance FTIR (ATR-FTIR), Raman, and XRD characterization instruments. These compounds are lithium acetate, lithium carbonate, <sup>6</sup>lithium fluoride, <sup>7</sup>lithium fluoride, lithium hydride, lithium hexafluorophosphate, lithium oxide, manganese(II) fluoride, nickel(II) fluoride, and polyethylene oxide (PEO). The online repository contains both the final and raw data, as well as the backgrounds removed. Our results both confirm and expand upon those already in the literature. This work, and connected data library, will aid researchers in their efforts to more efficiently identify, or exclude, potential SEI components via data analyses of complex spectra, and thus facilitate basic research of electrochemical interfaces of vital importance to battery materials science.

## Methods

Each of the three empirical characterization methods used – FTIR, Raman, and XRD – are detailed in the forthcoming subsections. Additionally, the protocols employed to ensure chemical compounds remained in an inert environment during storage, transfer, and characterization will also be briefly summarized, and fully validated in the Technical Validation section. Prior to any characterization, all pristine compounds were stored in an argon glovebox with base oxygen and water concentrations of ~0.1 ppm and ~0.5 ppm, respectively, and the sources and purities of the studied chemicals are provided in Table 1.

**Table 1**

Source and purity of compounds used for measurements presented in this paper

Chemical Name	Chemical Formula	Purity	Supplier	CAS Number
Lithium acetate	CH <sub>3</sub> COOLi	99.9%	Sigma Aldrich	546-89-4
Lithium carbonate	Li <sub>2</sub> CO <sub>3</sub>	99.999%	Sigma Aldrich	554-13-2
<sup>6</sup> Lithium fluoride	<sup>6</sup> LiF	99% <sup>a</sup>	Sigma Aldrich	14885-65-5
<sup>7</sup> Lithium fluoride	<sup>7</sup> LiF	99.99% <sup>b</sup>	Sigma Aldrich	7789-24-4
Lithium hydride	LiH	95%	Sigma Aldrich	7580-67-8
Lithium hexafluorophosphate	LiPF <sub>6</sub>	98%	Thermo Fisher Scientific	21324-40-3
Lithium oxide	Li <sub>2</sub> O	99.5%	Thermo Fisher Scientific <sup>c</sup>	12057-24-8
Manganese(II) fluoride	MnF <sub>2</sub>	99%	Thermo Fisher Scientific	7782-64-1
Nickel(II) fluoride	NiF <sub>2</sub>	97%	Thermo Fisher Scientific	10028-18-9
Polyethylene oxide	H(OCH <sub>2</sub> CH <sub>2</sub> ) <sub>n</sub> OH	100%	Thermo Fisher Scientific	25322-68-3

a) Advertised 95 atom percent <sup>6</sup>Li, with total compound purity of 99%

b) Advertised average molecular weight of 25.94 implies 92.6 atom percent <sup>7</sup>Li, with total compound purity of 99.99%

c) FTIR data taken using powder from American Elements (99.5%, LI-OX-025M-P)

**ATR-FTIR Spectroscopy.** ATR-FTIR spectra were collected using a Shimadzu IRTracer-100 instrument with an IRIS single reflection diamond accessory from 370 to 4000 cm<sup>-1</sup> at a spectral resolution of 2 cm<sup>-1</sup>. The instrument was housed in a nitrogen-filled glovebox with an oxygen concentration below 20 ppm. After being transferred into the ATR-FTIR enclosure in sealed vials, compounds were immediately placed on a clean diamond crystal for the ATR-FTIR measurement. This transfer approach was effective at minimizing unwanted reactions, as described in detail in the Technical Validation section below. Most compounds were measured using an average of 512 individual spectra (CH<sub>3</sub>COOLi, Li<sub>2</sub>CO<sub>3</sub>, <sup>7</sup>LiF, <sup>6</sup>LiF, Li<sub>2</sub>O, PEO) to maximize the signal to noise ratio, while only 50 spectra were accumulated for some of the more reactive compounds (LiH, LiPF<sub>6</sub>, MnF<sub>2</sub>, NiF<sub>2</sub>) to minimize acquisition time and thereby reduce the likelihood of undesired reactions.

**Raman Spectroscopy.** Raman spectra were collected using a 2 cm-square and 5 mm thick custom-made polyether ketone (PEEK) cell with an optical window (2.5 cm-square and 1 mm thick glass microscope slide). An illustration of the cell is provided in Fig. 1a, and it kept samples in an inert argon environment during measurement. Prior to cell assembly, PEEK cell bodies and glass slides were sequentially sonicated with acetone and isopropyl alcohol, and baked at 40°C for at least 4 hours, before being transferred into the glovebox for assembly. After a cell was assembled, it was enclosed within a heat-sealed bag, before being transferred to a Renishaw Qontor Raman microscope where Raman spectroscopy was conducted. A 488 nm excitation laser used, along with a spectral range of 100 to 3200 cm<sup>-1</sup>, 25 acquisitions, and laser power ranging from 1 to 10 mW. Unwanted contributions to the Raman spectra from the glass optical window were avoided by focusing the laser on the surface of the compounds.

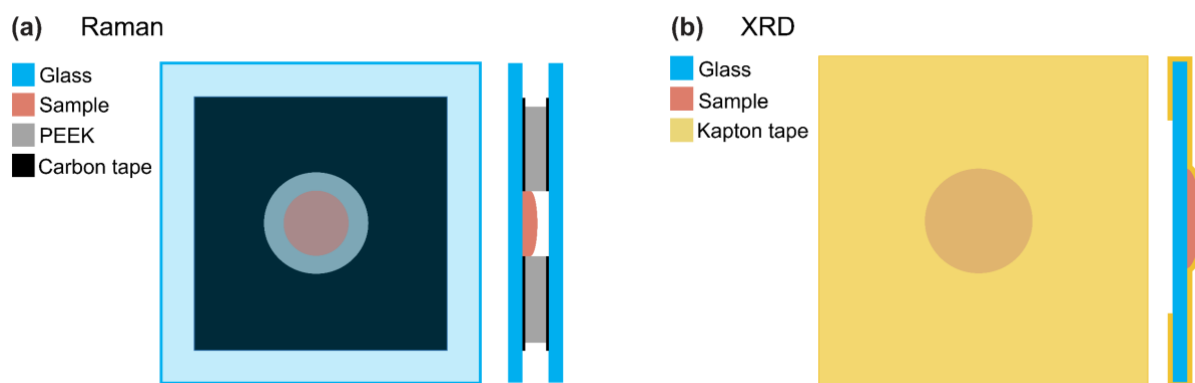


Fig. 1. Cell designs for (a) Raman and (b) XRD measurements.

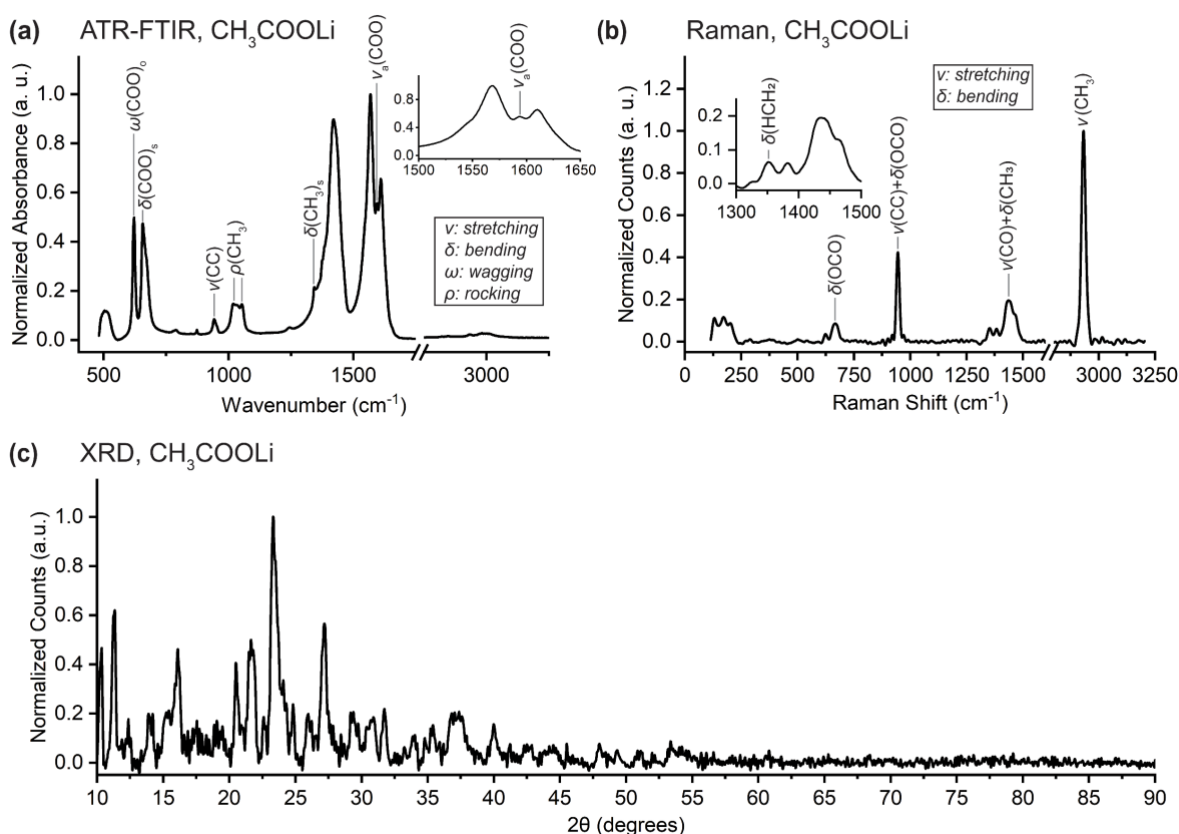
**X-Ray Diffraction.** Samples for XRD measurements were similarly assembled in the argon glovebox. Each compound was placed on a clean 2.5 cm-square and 1 mm thick glass microscope slide (cleaned and dried using the method described above) and covered with several sealing overlayers of polyimide tape (Kapton, Ted Pella, silicone adhesive, 70  $\mu\text{m}$  thick) before being heat-sealed in individual plastic bags. These sealed samples were then transferred to a Bruker Phaser D2 instrument to collect X-ray diffraction patterns over a  $2\theta$  range of 10 to 90 degrees, acquisition time of 0.2 seconds per step, and a step size of 0.02 degrees per step. All samples remained in their sealed bags until right before the start of measurement. XRD patterns were collected through the tape, rather than through glass, to prevent significant XRD contributions from the glass crystal. The amorphous background from the tape was removed via processing as described below in the Data Processing subsection. Comparison of our measurement of  $\text{Li}_2\text{O}$  to the results of Weber *et al.*<sup>19</sup> provides strong evidence that this approach successfully minimized unwanted reactions (see Technical Validation section).

**Data Processing.** The raw collected data was processed to remove unwanted instrumental and/or background contributions. Polynomials or Gaussians were fitted through the low wavenumber background in ATR-FTIR measurements. Spikes in the Raman spectra attributable to cosmic ray excitation were manually removed from Raman spectra. Subsequently, Raman spectra were then processed through the subtraction of Gaussian and/or polynomial fits to eliminate background contributions arising from a number of phenomena (e.g. fluorescence, glass effects, surface roughness). Our instrument generated raw Raman data with unevenly spaced wavenumber values, so an interpolation was performed to transform the data. Gaussian fits to determine peak positions from the data before and after interpolation confirmed transformation did not affect spectral feature shapes and centers. Gaussian fits were used to subtract out an amorphous background in XRD measurements generated by the Kapton tape. This background between 10 and 30 degrees appeared in all measurements through Kapton tape (but not in control measurements of bare metal foils) and was lower than the first diffraction peak of most compounds, allowing for a consistent background subtraction for measurements of the few compounds (like lithium acetate) where the first diffraction peak was found below 30 degrees. For all data types, Fourier filtering was applied to reduce high frequency noise (with care taken to avoid distorting spectral features) and small vertical offsets were used in some cases to align the final baseline near zero. All data was normalized to take on values from 0 to 1.

**Mode Assignment and Notation.** One of the goals and intended contributions of this work is to synthesize existing knowledge about the vibrational modes of the studied compounds, and

we make these identifications on plotted data in figures and in accompanying tables. We standardize the notation used to identify peaks where possible; we provide the type of vibrational mode, the bond or functional group that generates the peak, and the symmetry of the vibration. Where this is not possible, we adopt the notation that has been used in the literature that we direct the reader to. References are made to resources that provide additional details regarding the assignment of vibrational modes to spectral features. Unless otherwise noted, the Greek letters are used to describe vibrational modes according to the following associations:  $\omega$ , wagging;  $\delta$ , bending;  $\nu$ , stretching;  $\rho$ , rocking;  $\tau$ , twisting. Subscripts “a” and “s” refer to asymmetric and symmetric modes, respectively. Similarly, the subscripts “i” and “o” refer to in-plane and out-of-plane modes, respectively. In the following subsections, we present the data organized according to alphabetical order of the compounds in question.

**Lithium Acetate -  $\text{CH}_3\text{COOLi}$ .** Lithium acetate has been identified as an SEI component in  $\text{Li-O}_2$  batteries<sup>20</sup> and batteries with silicon anodes.<sup>21</sup> The FTIR spectrum in Fig. 2a is in agreement with spectra reported elsewhere.<sup>22-26</sup> We provide assignments for most peaks in the Fig., and in Table 2. The source of the peaks at 1421, 1568, and 1610  $\text{cm}^{-1}$  remains unknown, although it has been proposed that they are generated by vibrational modes of the carboxylate group ( $\text{COO}^-$ ).<sup>22</sup> Our data shows the presence of peaks at 503, 621, and 657  $\text{cm}^{-1}$  which have occasionally been reported in the literature.<sup>24,25</sup> There is some disagreement in the literature as to the shape of the peak near 1600  $\text{cm}^{-1}$ , and our results agree best with those of Ross<sup>26</sup> and Beyer *et al.*<sup>23</sup> The Raman spectrum in Fig. 2b is in good agreement with the literature, where more detailed peak identifications (as well as empirical peak locations for lithium acetate dihydrate and the free acetate ion) can be found.<sup>27,28</sup> Peak identifications are made in the figure and in Table 2. The XRD pattern in Fig. 2c is in good agreement with that of the anhydrous polymorph obtained from the dehydration of  $\text{CH}_3\text{COOLi}\cdot 2\text{H}_2\text{O}$ .<sup>29</sup> Note that there is substantial variation within the literature as to the XRD pattern of lithium acetate, in part due



to the dependency of the crystal structure on the specific hydrate (lithium acetate monohydrate and dihydrate as well as others) used as a precursor<sup>29</sup> and also possibly due to differences in sample preparation procedures that resulted in varying degrees of isolation from water and oxygen.

Fig. 2. (a) ATR-FTIR, (b) Raman, and (c) XRD data for lithium acetate (CH<sub>3</sub>COOLi). Labels for panels (a) are taken from Cadene<sup>30</sup> and for (b) from Sánchez-Carrera and Kozinsky<sup>27</sup> and Ananthanarayanan.<sup>28</sup>

**Table 2**

Peak assignments for FTIR and Raman spectra of lithium acetate

FTIR		
This work (cm <sup>-1</sup> )	Literature <sup>30</sup> (cm <sup>-1</sup> )	Assignment
621	621	$\omega(\text{COO})_o$
657	660	$\delta(\text{COO})_s$
942	943	$\nu(\text{CC})$
1020	1031	$\rho(\text{CH}_3)$
1053	1055	$\rho(\text{CH}_3)$
1343	1348	$\delta(\text{CH}_3)_s$
1594	1595	$\nu_a(\text{COO})$
Raman		
This work (cm <sup>-1</sup> )	Literature <sup>27</sup> (cm <sup>-1</sup> )	Assignment
Excitation wavelength: 488 nm	Calculated	
667	-	<sup>a</sup> $\delta(\text{OCO})$
946	[942]	$\nu(\text{CC}) + \delta(\text{OCO})$
1352	[1387]	$\delta(\text{HCH}_2)$
1435	[1440]	$\nu(\text{CO}) + \delta(\text{CH}_3)$
2933	[2953]	$\nu(\text{CH}_3)$

Note: Empirical locations of Raman peaks in lithium acetate dihydrate and the free acetate ion available in Ananthanarayanan.<sup>28</sup>

a) Assignment inferred from Ananthanarayanan<sup>28</sup>

**Lithium Carbonate, Li<sub>2</sub>CO<sub>3</sub>.** Lithium carbonate forms in the anodic SEI of LIBs through the decomposition of ethylene carbonate<sup>31</sup> and is also often found on the surface of lithium metal following native passivation.<sup>32</sup> The ATR-FTIR spectrum, reported in Fig. 3a, closely matches most of those previously reported.<sup>23,33-36</sup> Although some spectra are truncated well above 500 cm<sup>-1</sup>, Özer *et al.*<sup>35</sup> and Pasierb *et al.*<sup>36</sup> report a strong peak near 500 cm<sup>-1</sup> and a weaker peak at slightly lower wavenumbers (both assigned to quasi-lattice vibrations<sup>36</sup>), similar to the peaks that we report at 477 and 408 cm<sup>-1</sup>. The Raman spectrum in Fig. 3b is in good agreement with the literature.<sup>36,37</sup> The peaks that we report in the low-wavenumber region (at 128, 156, 194, and 274 cm<sup>-1</sup>) can be attributed to translational or rotational lattice vibrations of the carbonate ion (CO<sub>3</sub><sup>2-</sup>).<sup>38,39</sup> Peak identifications for FTIR and Raman-active vibrational modes are made in the figure and in Table 3. Additional information about vibrational modes can be found in Brooker and Bates,<sup>40</sup> Brooker and Wang,<sup>41</sup> and Hase and Yoshida.<sup>38</sup> The XRD pattern in Fig. 3c confirms peak positions found in the literature and is consistent with a monoclinic crystal structure.<sup>42-44</sup> We report relative peak intensities that differ somewhat from previously

reported values, although these values in the literature are generally not consistent with each other. Of note are the smaller peaks between 55 and 60 degrees, whose positions and relative intensities have not been agreed upon and which have been assigned to different crystal planes.<sup>42,44</sup>

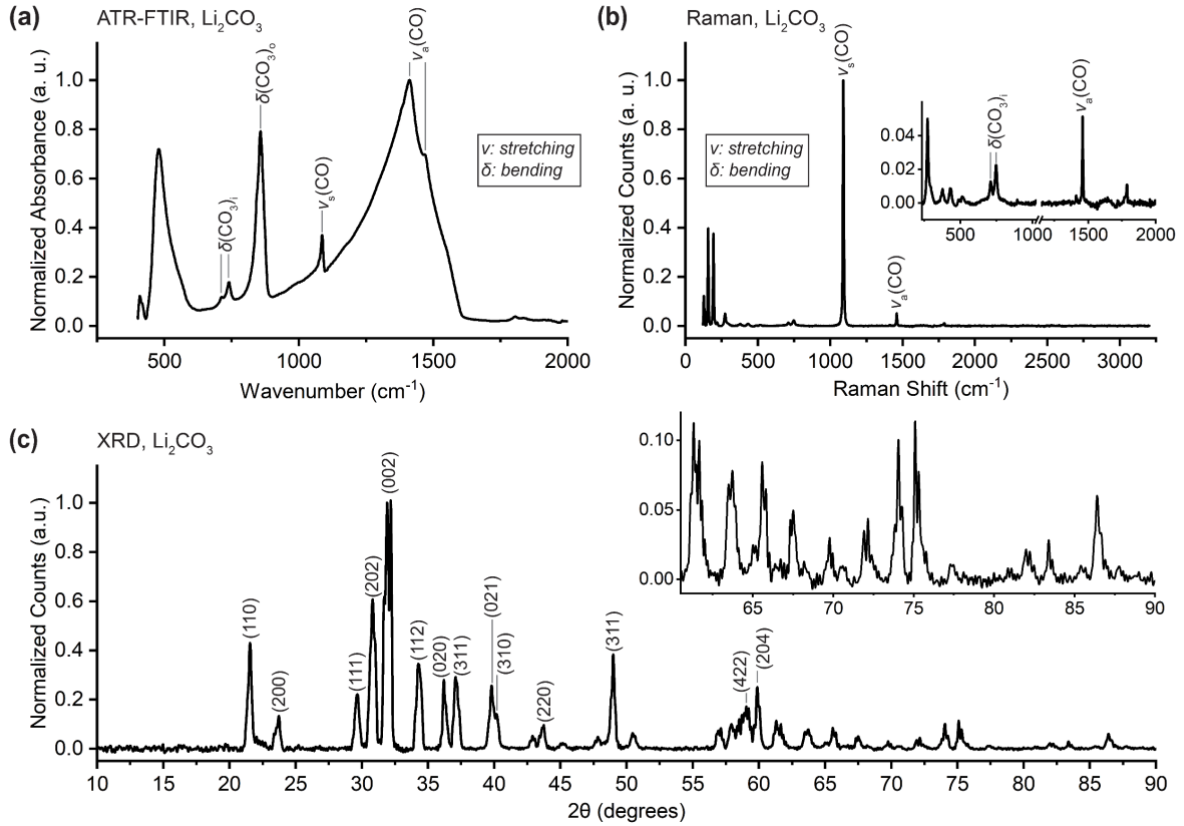


Fig. 3. (a) ATR-FTIR, (b) Raman, and (c) XRD data for lithium carbonate ( $\text{Li}_2\text{CO}_3$ ). Labels are taken from the literature: (a) and (b) Pasierb *et al.*<sup>36</sup> and (c) Chen *et al.*<sup>44</sup>

**Table 3**  
Peak assignments for FTIR and Raman spectra of lithium carbonate

FTIR		
This work ( $\text{cm}^{-1}$ )	Literature <sup>36</sup> ( $\text{cm}^{-1}$ )	Assignment
713	712	$\delta(\text{CO}_3)_i$
740	748	$\delta(\text{CO}_3)_i$
857	863	$\delta(\text{CO}_3)_o$
1087	1088	$\nu_s(\text{CO})$
1412	1437	$\nu_a(\text{CO})$
1468	1503	$\nu_a(\text{CO})$
Raman		
This work ( $\text{cm}^{-1}$ )	Literature <sup>36</sup> ( $\text{cm}^{-1}$ )	Assignment
Excitation wavelength: 488 nm		
710	712	$\delta(\text{CO}_3)_i$
748	748	$\delta(\text{CO}_3)_i$
1090	1088	$\nu_s(\text{CO})$
1459	1458	$\nu_a(\text{CO})$
Excitation wavelength: 1064 nm		

**Lithium Fluoride -  $^7\text{LiF}$  &  $^6\text{LiF}$ .** Lithium fluoride is a primary component of the initial SEI in LIBs and is produced when  $\text{LiPF}_6$  is reduced during a reaction with ethylene carbonate.<sup>31,45</sup> Both  $^7\text{LiF}$  and  $^6\text{LiF}$  are naturally occurring to some extent and their vibrational spectra are expected to be influenced by their differing atomic weights.<sup>46,47</sup> The ATR-FTIR spectra in Fig. 4a are similar to each other in that they have broad double peaks in the low wavenumber region. However, the peaks of the lighter  $^6\text{LiF}$ , at 527 and 595  $\text{cm}^{-1}$ , are shifted approximately 20  $\text{cm}^{-1}$  higher than those of  $^7\text{LiF}$  (at 508 and 568  $\text{cm}^{-1}$ ), in accordance with well-established theory about the effect of isotope masses on the frequency of vibrational modes.<sup>46</sup> These features contrast with identifications, including a sharp peak near 800  $\text{cm}^{-1}$  attributed to LiF elsewhere, and those in spectra of LiF collected at high temperature while within an argon matrix.<sup>48,49</sup> While Raman data was collected, we do not plot it here because high fluorescence overwhelmed features of interest. The raw data is made available in the Dryad repository. As seen in Fig. 4c, both compounds have XRD patterns that are consistent with their cubic structure and are in accordance with the literature.<sup>50-52</sup> Note that data is often reported only through 80 degrees, excluding the peak at 83 degrees assigned to the 222 crystal plane.<sup>53</sup> We find that the diffraction peaks of  $^6\text{LiF}$  are shifted slightly higher than those of  $^7\text{LiF}$ , which would be qualitatively consistent with expected isotope effects, albeit this shift is somewhat larger than what may be expected.<sup>54</sup> Diffraction peaks for  $^7\text{LiF}$  around 79 and 83 degrees are assigned to the 311 and 222 crystal planes in the literature, and we extend these assignments to  $^6\text{LiF}$  on the basis of their shared cubic crystal structure and very similar unit cell size.



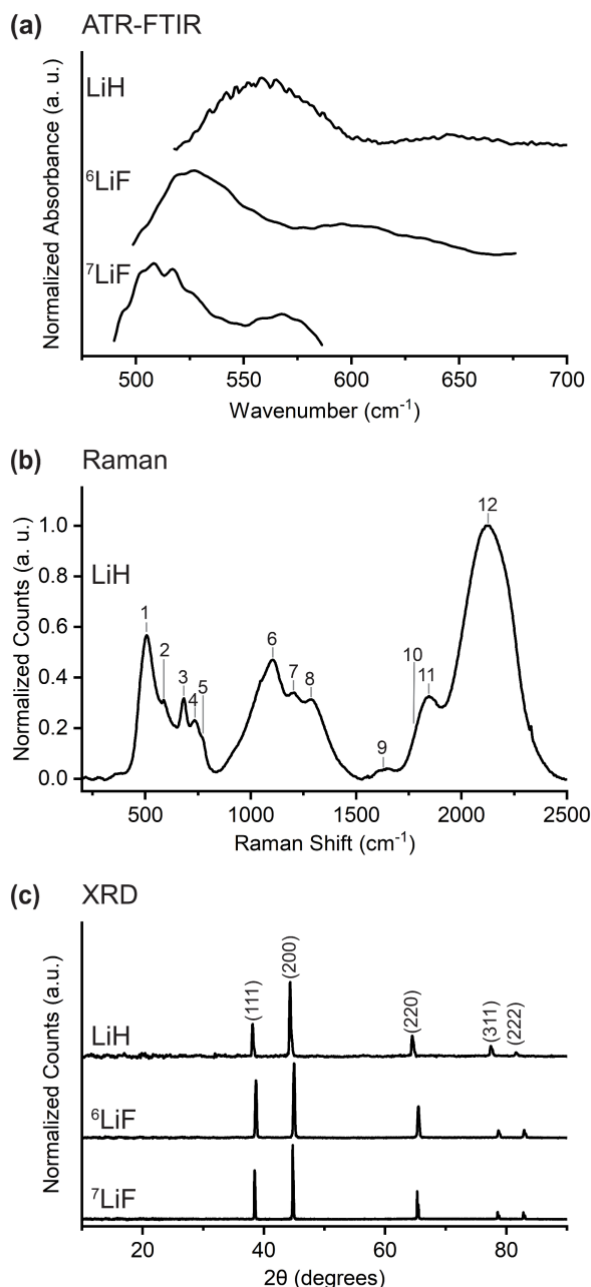


Fig. 4. (a) ATR-FTIR, (b) Raman, and (c) XRD data for lithium fluoride (<sup>7</sup>LiF and <sup>6</sup>LiF) and lithium hydride (LiH). Numeric labels in panel (b) correspond to linear combinations of optical and acoustic modes in the LiH crystal as detailed in Tyutyunnik and Tyutyunnik.<sup>55</sup> Labels in panel (c) apply to all three compounds and are from the following sources: LiH labels from Weber *et al.*,<sup>56</sup> <sup>6</sup>LiF labels from Carturan *et al.*,<sup>57</sup> and <sup>7</sup>LiF labels from Zhang *et al.*<sup>51</sup> and Paterson.<sup>53</sup>

**Lithium Hydride – LiH.** Lithium hydride is a common component of the SEI in lithium-anode batteries and has been identified in lithium dendrites in LIBs, including dendrites composed primarily of LiH that are associated with substantial capacity fading.<sup>58</sup> Importantly, LiH is sometimes misidentified as LiF due to similarities in their chemical properties, underscoring the importance of having quality reference data for both compounds provided in a single location.<sup>59</sup> The ATR-FTIR spectrum in Fig. 4a contains peaks at 558 and 646 cm<sup>-1</sup>; the shift to higher wavenumber relative to the heavier lithium fluoride is consistent with theoretical

expectations.<sup>46</sup> The main peak location aligns with a previously reported spectra, although we may be the first to report the weak secondary peak at 648 cm<sup>-1</sup>.<sup>60</sup> The Raman spectra in Fig. 4b reproduces existing spectra and confirms that the sample has not reacted with water to form Li<sub>2</sub>O or LiOH.<sup>55,61</sup> Peak assignments are adopted from Tyutyunnik and Tyutyunnik<sup>55</sup> and the peak label “10” indicates the location where they find a modest peak that we do not observe in our data. Raman peak locations and assignments are also provided in Table 4. As seen in Fig. 4c, lithium hydride produces an XRD pattern similar to that of lithium fluoride, likely due to their cubic crystal structures and comparable unit cell sizes. This is consistent with the literature.<sup>56,60,62</sup> The absence of peaks at 33 and 56 degrees (attributed to Li<sub>2</sub>O) confirms the pristine nature of LiH.<sup>56</sup>

**Table 4**  
Peak assignments for Raman spectrum of lithium hydride

This work (cm <sup>-1</sup> ) Excitation wavelength: 488 nm	Literature <sup>55</sup> (cm <sup>-1</sup> ) Excitation wavelength: 514.5 nm	Assignment
514	511	1
592	586	2
688	687	3
748	736	4
779	776	5
1094	1109	6
1221	1211	7
1305	1293	8
1649	1638	9
-	1736	10
1833	1835	11
2142	2113	12

Note: Detailed peak identifications provided in the reference<sup>55</sup>

**Lithium Hexafluorophosphate - LiPF<sub>6</sub>.** Lithium hexafluorophosphate is commonly used as a lithium source in liquid electrolytes of LIBs. As a result, residual salt is commonly found on and in the SEI, especially after the evaporation of the volatile components of the electrolyte.<sup>63</sup> The ATR-FTIR spectrum is provided in Fig. 5a. Peak assignments in Fig. 5 and Table 5 adopt the notation that is consistently used in the literature. Note that Pekarek *et al.*<sup>64</sup> assign the peaks that they observe at 559 and 871 cm<sup>-1</sup> to  $\delta_s(\text{FPF})$  and  $\nu_s(\text{PF})$ , respectively. The Raman spectrum in Fig. 5b is in excellent agreement with previously reported values and peak identifications are provided in Table 5.<sup>65-67</sup> The  $\nu_1$  vibrational mode at 771 cm<sup>-1</sup> has been identified as arising from a P-F symmetric stretching mode.<sup>68</sup> It is worth noting that the normal modes of vibration of the PF<sub>6</sub><sup>-</sup> ion are dependent on the coordination of the ion and so can be expected to vary according to the local chemistry of a given SEI.<sup>68</sup> Moreover, partial oxidation of the PF<sub>6</sub><sup>-</sup> ion (which can occur upon electrochemical cycling) can also lead to changes in the position of the primary peaks.<sup>65</sup> Presented in Fig. 5c, the peak locations in the XRD pattern are in good agreement with the literature.<sup>65,67,69</sup> Further, we find relative peak intensities that fall in the wide range of results reported by others, with exception of a much stronger peak at 52 degrees than is reported elsewhere. There is some disagreement in the literature as to the crystal structure of LiPF<sub>6</sub>; Liu *et al.*<sup>69</sup> suggest a hexagonal crystal structure and Kock *et al.*<sup>65</sup> use Raman data to propose a cubic crystal structure like that of NaPF<sub>6</sub> and KPF<sub>6</sub>.

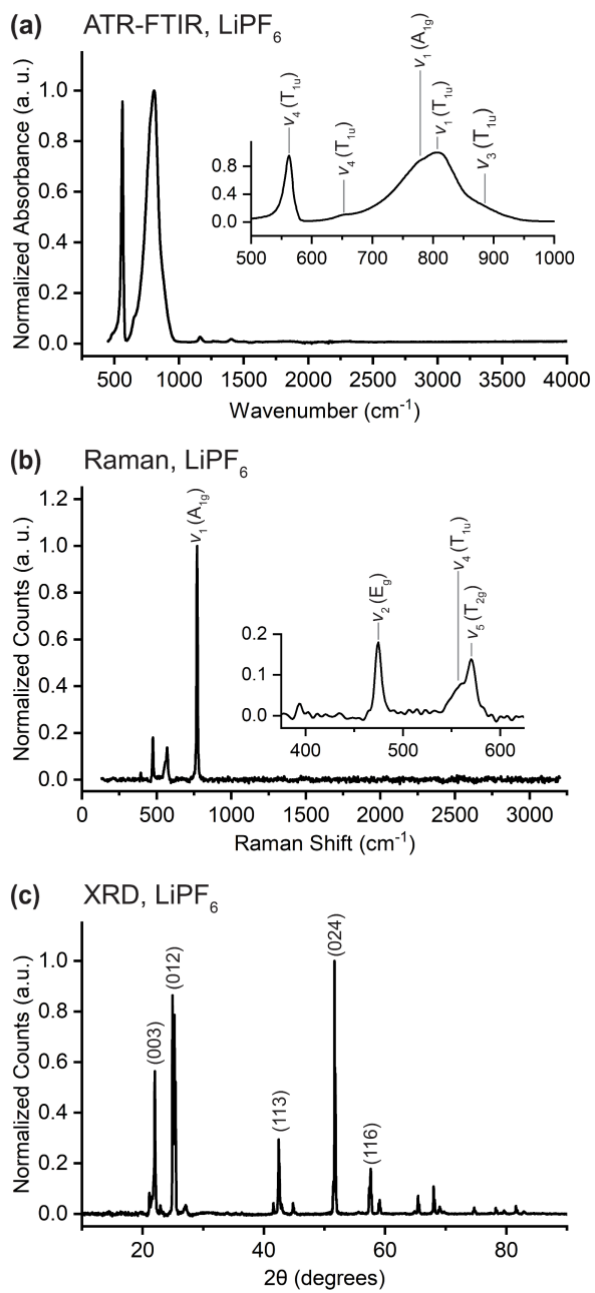


Fig. 5. (a) ATR-FTIR, (b) Raman, and (c) XRD data for lithium hexafluorophosphate (LiPF<sub>6</sub>). Labels from the literature: (a) and (b) from Kock *et al.*<sup>65</sup> and (c) from Masoud *et al.*<sup>70</sup>

**Table 5**

Peak assignments for FTIR and Raman spectra of lithium hexafluorophosphate

FTIR		
This work (cm <sup>-1</sup> )	Literature <sup>65</sup> (cm <sup>-1</sup> )	Assignment
561	560	$\nu_4$ (T <sub>1u</sub> )
650	646	$\nu_4$ (T <sub>1u</sub> )
778	775	$\nu_1$ (A <sub>1g</sub> )
805	798	$\nu_1$ (T <sub>1u</sub> )
887	869	$\nu_3$ (T <sub>1u</sub> )
Raman		
This work (cm <sup>-1</sup> )	Literature <sup>65</sup> (cm <sup>-1</sup> )	Assignment
Excitation wavelength: 488 nm	Excitation wavelength: 1064 nm	
475	475	$\nu_2$ (E <sub>g</sub> )
561	560	$\nu_4$ (T <sub>1u</sub> )
571	571	$\nu_5$ (T <sub>2g</sub> )
771	771	$\nu_1$ (A <sub>1g</sub> )

Note: Notation adopted from Kock *et al.*<sup>65</sup>

**Lithium Oxide - Li<sub>2</sub>O.** Lithium oxide is believed to form in the SEI as a decomposition product of lithium ethylene dicarbonate<sup>31</sup> and also forms on the surface of lithium metal via native passivation.<sup>32</sup> It can be difficult to obtain pristine spectra of lithium oxide; not only because it reacts readily with water, but also because it is typically offered by vendors with some existing contamination/inpurity.<sup>19</sup> While absorption features were observed at higher wavenumber values, ATR-FTIR data of Li<sub>2</sub>O is presented here in Fig. 6a below 800 cm<sup>-1</sup> to focus on Li<sub>2</sub>O-specific features, which are fairly consistent with sparse reports in the literature (e.g. in the supplemental section of Tian *et al.*<sup>71</sup>). In order to verify infrared spectral features originating strictly from Li<sub>2</sub>O vibrations, we collected a number of spectra of powders exposed for various amounts of time to gaseous water, CO<sub>2</sub>, and/or heating at 400 °C (to dehydrate the sample). As a result, features attributable to Li<sub>2</sub>CO<sub>3</sub> (870, 1432, and 1499 cm<sup>-1</sup>)<sup>71-73</sup> and LiOH (3523, 3676 cm<sup>-1</sup>)<sup>74</sup> were identified. These features scaled with exposure to moisture and CO<sub>2</sub> at room temperature. However, and interestingly, one absorption feature associated with LiOH (3523 cm<sup>-1</sup>) was found to decrease in intensity with increasing dehydration by way of heating. Thus, and in accord with past reports, the weak peak at ca. 3523 cm<sup>-1</sup> is assigned to LiOH·H<sub>2</sub>O,<sup>75,76</sup> while the peak at 3676 cm<sup>-1</sup> is assigned to the O-H stretching mode in LiOH. Ultimately, all these “impurities” were found above 800 cm<sup>-1</sup>, hence our choice of scale in Fig. 6a.

The Raman spectrum of lithium oxide is provided in Fig. 6b. The feature at 523 cm<sup>-1</sup> of the main Li-O vibration (in the  $F_{2g}$  symmetry group<sup>77</sup>) is congruent with the range of peak positions, from 515 to 529 cm<sup>-1</sup>, reported in the literature<sup>19,78</sup> (including the Supplemental Materials section of Gittleson *et al.*<sup>79</sup>) and precisely confirms the experimental result of Sánchez-Carrera and Kozinsky<sup>27</sup> and Osaka and Shindo.<sup>77</sup> The variance in the previously reported peak locations may be due to differences in the excitation laser wavelength used, as seen in Table 6, although we observe the same peak position when using a 488 and 633 nm excitation lasers. We present the collected XRD pattern, which is in good agreement with data reported elsewhere, in Fig. 6b.<sup>80,81</sup> This pattern is consistent with a cubic crystal structure.

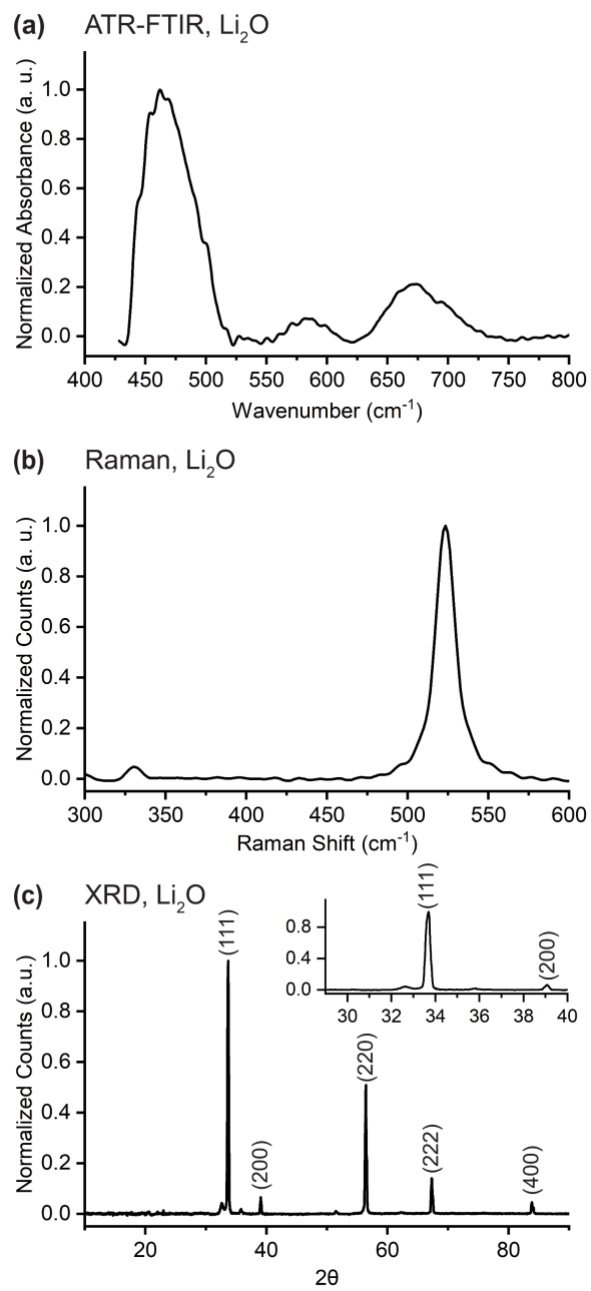


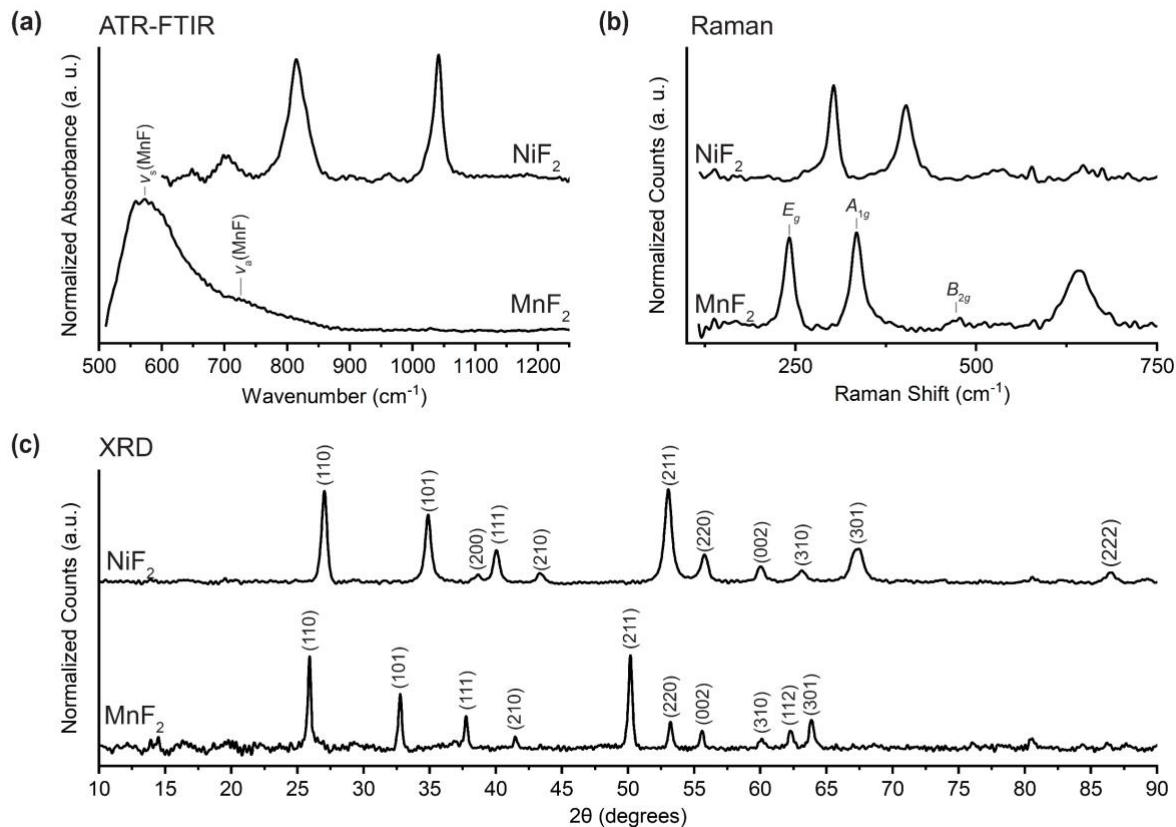
Fig. 6. (a) FTIR, (b) Raman, and (c) XRD data for lithium oxide ( $\text{Li}_2\text{O}$ ). Labels for panel (c) from the Materials Project.<sup>82</sup>

**Table 6**

Primary Raman peak location of lithium oxide

Excitation Wavelength (nm)	Primary Peak Location (cm <sup>-1</sup> )	Reference
325	515	Sifuentes <i>et al.</i> <sup>78</sup>
488	523	This work
488	523	Osaka and Shindo <sup>77</sup>
514.5	523	Osaka and Shindo <sup>77</sup>
532	527	Weber <i>et al.</i> <sup>19</sup>
633	523	This work
785	529	Gittleson <i>et al.</i> <sup>79</sup>

**Manganese(II) Fluoride - MnF<sub>2</sub>.** Manganese(II) fluoride may form in the SEI on manganese-containing metallic glass anodes following reactions with LiPF<sub>6</sub> salt in the electrolyte<sup>83</sup> and on other manganese-rich electrodes.<sup>84-86</sup> The ATR-FTIR spectrum presented in Fig. 7a contains peaks similar to those calculated and empirically reported in Scholz and Stösser<sup>87</sup> as seen in Table 7. We find a peak at 575 cm<sup>-1</sup> that may be generated by the symmetric stretching mode whose position they calculated but which they did not experimentally report.<sup>87</sup> The Raman spectrum in Fig. 7b agrees closely with previously reported values.<sup>88</sup> We provide the symmetry groups of the phonon modes believed to generate the peaks in the low wavenumber region. The peak at 641 cm<sup>-1</sup> remains unassigned. Seen in Fig. 7c, XRD suggests a tetragonal structure and is in good agreement with published patterns.<sup>89-91</sup> While relative peak intensities are generally similar to those found in the literature, the peak at 50 degrees is somewhat stronger than reported elsewhere.

Fig. 7. (a) ATR-FTIR, (b) Raman, and (c) XRD data for manganese(II) fluoride (MnF<sub>2</sub>) and nickel(II)

fluoride (NiF<sub>2</sub>). Labels from the literature: (a) Scholz and Stösser,<sup>87</sup> (b) Stavrou *et al.*,<sup>88</sup> (c) Rui *et al.*<sup>89</sup> for MnF<sub>2</sub>, (c) Jiao *et al.*<sup>92</sup> for NiF<sub>2</sub>.

**Table 7**

Peak assignments for FTIR and Raman spectra of manganese(II) fluoride

FTIR		
This work (cm <sup>-1</sup> )	Literature <sup>87</sup> (cm <sup>-1</sup> )	Assignment
575	--- [529-599]	v <sub>s</sub> (MnF)
726	700 [673-768]	v <sub>a</sub> (MnF)
Raman		
This work (cm <sup>-1</sup> ) Excitation wavelength: 488 nm	Literature <sup>88</sup> (cm <sup>-1</sup> ) Excitation wavelength: 488 nm	Assignment (Phonon Mode) <sup>a</sup>
247	245 [233]	E <sub>g</sub>
341	340 [350]	A <sub>1g</sub>
476	457 [463]	B <sub>2g</sub>

Note: Calculated frequencies in square brackets

a) Raman peak identifications refer to phonon modes.

**Nickel(II) Fluoride - NiF<sub>2</sub>.** Nickel(II) fluoride is believed to form in the SEI on lithium nickel cobalt manganese oxide cathodes in LIBs.<sup>93,94</sup> There is substantial disagreement in the literature as to the correct FTIR spectrum; our data is shown in Fig. 7a and most closely matches that of Tramšek *et al.*<sup>95</sup> with primary peaks at 817 and 1043 cm<sup>-1</sup>. Note that Tramšek *et al.* report weak peaks similar to those that we find at 651 and 706 cm<sup>-1</sup> but that they are more prominent in our data due to our use of a background subtraction. Presented in Fig. 7b, our Raman spectrum shows peaks at 303 and 405 cm<sup>-1</sup> in good agreement with Ullah *et al.*<sup>96</sup> The XRD pattern in Fig. 7c closely matches those reported in the literature with respect to both peak locations and relative intensities (with the exception of the strong peak that we report at 53 degrees) and is consistent with the expected tetragonal structure.<sup>92,97,98</sup> Note that the broad peak near 67 degrees has been suggested to be two adjacent peaks stemming from the 301 and 112 crystal planes but we do not have sufficient resolution to make this identification.<sup>97</sup>

**Polyethylene oxide - H(OCH<sub>2</sub>CH<sub>2</sub>)<sub>n</sub>OH.** Polyethylene oxide is a polymer used in polymer electrolytes and as a component in artificial SEIs for anode-free batteries.<sup>99,100</sup> PEO oligomers have also been identified as naturally forming components of the SEI on silicon anodes and are believed to be products of electrolyte reduction.<sup>101</sup> Seen in Fig. 8a, the FTIR spectrum that we present contains the low-wavenumber peaks at 509 and 530 cm<sup>-1</sup> and the peak at 2876 cm<sup>-1</sup> reported in some works<sup>102-105</sup> but only faintly shows the broad feature near 3370 cm<sup>-1</sup> found by some<sup>102-104</sup> but not others.<sup>105,106</sup> Peak locations and vibrational mode assignments are provided in the figure and in Table 8; phase relations of “+” and “-” are provided for coupled coordinates where available but are otherwise replaced with a comma. Additional discussions of vibrational modes can be found in the literature.<sup>107</sup> The Raman spectrum presented in Fig. 8b is in good agreement with the existing literature.<sup>108-110</sup> The XRD pattern in Fig. 8c aligns well with those reported in the literature.<sup>111-113</sup>

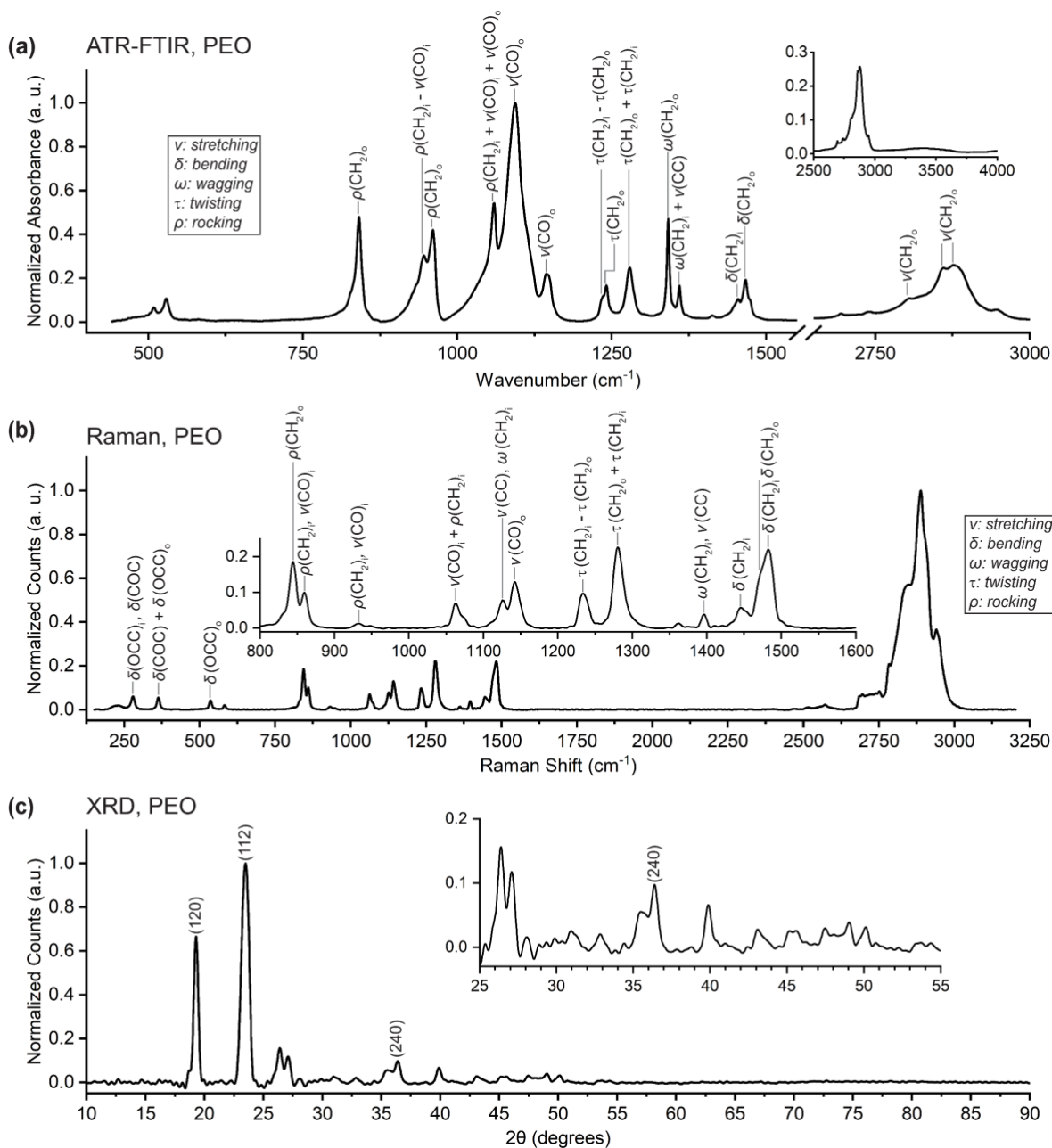


Fig. 8. (a) ATR-FTIR, (b) Raman, and (c) XRD data for polyethylene oxide (H(OCH<sub>2</sub>CH<sub>2</sub>)<sub>n</sub>OH). Labels from the literature: (a) Matsui *et al.*<sup>114</sup> and Ratna *et al.*,<sup>115</sup> (b) Matsui *et al.*<sup>114</sup> and (c) Telfah *et al.*<sup>116</sup> Phase relations of “+” and “-” are provided for coupled coordinates where available but are otherwise replaced with a comma.



**Table 8**

Peak assignments for FTIR and Raman spectra of polyethylene oxide

FTIR		
This work (cm <sup>-1</sup> )	Literature <sup>114,115</sup> (cm <sup>-1</sup> )	Assignment
841	844 [856]	$\rho(\text{CH}_2)_o$
946	947 [924]	$\rho(\text{CH}_2)_i - \nu(\text{CO})_i$
961	958 [884]	$\rho(\text{CH}_2)_o$
1060	1060 [1033]	$\rho(\text{CH}_2)_i + \nu(\text{CO})_i + \nu(\text{CO})_o$
1094	1103 [1061]	$\nu(\text{CO})_o$
1144	1147 [1161]	$\nu(\text{CO})_o^*$
1236	1234 [1250]	$\tau(\text{CH}_2)_i - \tau(\text{CH}_2)_o$
1241	1240 [1280]	$\tau(\text{CH}_2)_o$
1279	1278 [1282]	$\tau(\text{CH}_2)_o + \tau(\text{CH}_2)_i$
1342	1342 [1386]	$\omega(\text{CH}_2)_o$
1360	1358 [1354]	$\omega(\text{CH}_2)_i + \nu(\text{CC})$
1454	1448 [1470]	$\delta(\text{CH}_2)_i$
1467	1466 [1474]	$\delta(\text{CH}_2)_o$
2806	2750-3000	$\nu(\text{CH}_2)_o$
2861	2750-3000	$\nu(\text{CH}_2)_o$
2876	2750-3000	$\nu(\text{CH}_2)_o$

Raman		
This work (cm <sup>-1</sup> )	Literature <sup>114</sup> (cm <sup>-1</sup> )	Assignment
Excitation wavelength: 488 nm	Excitation wavelength: 435.8 nm	
279	274 [270]	$\delta(\text{OCC})_i, \delta(\text{COC})$
363	359 [366]	$\delta(\text{COC}) + \delta(\text{OCC})_i$
536	531 [501]	$\delta(\text{OCC})_o^*$
844	844 [856]	$\rho(\text{CH}_2)_o$
860	859 [876]	$\rho(\text{CH}_2)_i, \nu(\text{CO})_i$
933	930 [924]	$\rho(\text{CH}_2)_i, \nu(\text{CO})_i$
1062	1066 [1093]	$\nu(\text{CO})_i + \rho(\text{CH}_2)_i$
1126	1130 [1138]	$\nu(\text{CC}), \omega(\text{CH}_2)_i$
1142	1147 [1161]	$\nu(\text{CO})_o^*$
1231	1237 [1250]	$\tau(\text{CH}_2)_i - \tau(\text{CH}_2)_o$
1280	1283 [1282]	$\tau(\text{CH}_2)_o + \tau(\text{CH}_2)_i$
1396	1398 [1381]	$\omega(\text{CH}_2)_i, \nu(\text{CC})$
1446	1447 [1470]	$\delta(\text{CH}_2)_i$
1470	1474 [1474]	$\delta(\text{CH}_2)_o$
1480	1483 [1473]	$\delta(\text{CH}_2)_i$

Note: Calculated frequencies in square brackets. Phase relations of “+” and “-” are provided for coupled coordinates where available but are otherwise replaced with a comma.  
\*Alternative identification is made in Tadokoro *et al.*<sup>107</sup>

## Data Records

All data presented or discussed herein can be found in the Dryad repository associated with this work. The data files are in a .xlsx format which can be opened using Excel (including the free Excel Viewer) and Google Sheets among other applications. These files can be saved out in a .csv or other format as desired for use in other software (including data processing and plotting programs). One Excel workbook file is provided for each characterization

technique (ATR-FTIR, Raman, and XRD). Each sheet contains data for one compound, whose identity is indicated by the chemical formula and written name. Raw and final data are provided, and the ATR-FTIR and XRD data files also contain an additional sheet with all final data on a single x axis. Note that final Raman data for  $^6\text{LiF}$  and  $^7\text{LiF}$  are omitted as discussed in the Methods section, and that raw Raman data has uneven x-axis spacing so had to be interpolated to apply the Fourier filter. There are therefore different wavenumber axes for the raw and final Raman data; the axes are provided in each sheet and are visually offset by an empty column. The .txt file in the repository folder contains a duplicate of the information provided in this section.

## Technical Validation

A primary consideration when designing the procedures outlined in the Methods section was to ensure the purity of the compounds that we measured. Our success in doing so was confirmed through the comparison of our data to literature results of both reacted and pristine compounds of interest. Comparison of the ATR-FTIR spectrum of  $\text{LiPF}_6$  (shown in Fig. 5a) to the literature demonstrates our measurement procedure's efficacy in preventing unwanted side reactions; the  $\text{LiPF}_6$  is demonstrably unreacted.<sup>65,67</sup> The efficacy of our Raman measurement protocols is supported by the lithium hydride spectrum in Fig. 4b; the absence of peaks at  $523\text{ cm}^{-1}$  (from  $\text{Li}_2\text{O}$ ) and between  $250$  and  $350\text{ cm}^{-1}$  (attributed to  $\text{LiOH}$ )<sup>61</sup> provides strong evidence that this highly oxygen- and water-sensitive compound has not formed its common reaction products. Further, the quality of the XRD data is confirmed through analysis of our lithium oxide data (in Fig. 6c); there are strong peaks generated by  $\text{Li}_2\text{O}$  with almost negligible contributions from the 101 plane of  $\text{LiOH}$  at  $\sim 32$  degrees (which have been suggested to arise from impurities in the as-delivered powder<sup>19</sup>) no detectable contributions from the 110 plane of  $\text{LiOH}\cdot\text{H}_2\text{O}$  at  $\sim 36$  degrees, indicating that the sample was well protected from oxygen and had no detectable exposure to water.<sup>19</sup> Further, the absence of peaks at 33 and 56 degrees in the XRD pattern of  $\text{LiH}$  in Fig. 4c confirms the absence of  $\text{LiOH}$  contamination in the  $\text{LiH}$ .<sup>56</sup>

Our data also closely aligns with previously reported spectra and patterns (where these are available) for FTIR (lithium acetate<sup>23,26</sup>, lithium carbonate<sup>35,36</sup>, lithium hydride<sup>60</sup>, lithium hexafluorophosphate<sup>65,67</sup>, nickel(II) fluoride<sup>95</sup>, polyethylene oxide<sup>106</sup>), Raman (lithium acetate<sup>27,28</sup>, lithium carbonate<sup>36,37</sup>, lithium hydride<sup>55</sup>, lithium hexafluorophosphate<sup>65-67</sup>, lithium oxide<sup>27,77</sup>, manganese(II) fluoride<sup>88</sup>, nickel(II) fluoride<sup>96</sup>, polyethylene oxide<sup>108-110</sup>), and XRD (lithium acetate<sup>29</sup>, lithium carbonate<sup>42-44</sup>,  $^6\text{lithium fluoride}$ <sup>52</sup>,  $^7\text{lithium fluoride}$ <sup>50,51</sup>, lithium hydride<sup>56,60,62</sup>, lithium hexafluorophosphate<sup>65,67,69</sup>, lithium oxide<sup>19,80,81</sup>, manganese(II) fluoride<sup>89-91</sup>, nickel(II) fluoride<sup>92,97,98</sup>, polyethylene oxide<sup>111-113</sup>) measurements.

## Acknowledgments

We kindly acknowledge sources that financially supported this work. Funding to support this work was provided by the Assistant Secretary for Energy Efficiency and Renewable Energy, Vehicle Technologies Office, under the Advanced Battery Materials Research (BMR) Program, of the U.S. Department of Energy under Contract No. DE-AC02-05CH11231. Additionally, funding to support this work was also provided by the Energy & Biosciences Institute through the EBI-Shell program.

## Author contributions

J.M.L. and R.K. supervised the work. J.M.L. conceived of the project concept. L. K.-S. prepared the samples and collected a vast majority of the data while being supported by A.S., A.D., M. I.-U.-H., H.C., and J.M.L. with sample storage and preparation advice, miscellaneous data collection, and training. L. K.-S. wrote and prepared the manuscript draft with J.M.L.'s

supervision and guidance. All authors contributed to the interpretation, conclusions, and preparation of the final manuscript.

## Competing interests

The authors declare no competing interests.

## References

- 1 Diouf, B. & Pode, R. Potential of lithium-ion batteries in renewable energy. *Renewable Energy* **76**, 375-380 (2015). <https://doi.org/10.1016/j.renene.2014.11.058>
- 2 Goodenough, J. B. & Park, K.-S. The Li-Ion Rechargeable Battery: A Perspective. *Journal of the American Chemical Society* **135**, 1167-1176 (2013). <https://doi.org/10.1021/ja3091438>
- 3 Li, W., Song, B. & Manthiram, A. High-voltage positive electrode materials for lithium-ion batteries. *Chem Soc Rev* **46**, 3006-3059 (2017). <https://doi.org/10.1039/c6cs00875e>
- 4 Ma, H., Balthasar, F., Tait, N., Riera-Palou, X. & Harrison, A. A new comparison between the life cycle greenhouse gas emissions of battery electric vehicles and internal combustion vehicles. *Energy Policy* **44**, 160-173 (2012). <https://doi.org/10.1016/j.enpol.2012.01.034>
- 5 Kousksou, T., Bruel, P., Jamil, A., El Rhafiki, T. & Zeraouli, Y. Energy storage: Applications and challenges. *Solar Energy Materials and Solar Cells* **120**, 59-80 (2014). <https://doi.org/10.1016/j.solmat.2013.08.015>
- 6 Hall, P. J. & Bain, E. J. Energy-storage technologies and electricity generation. *Energy Policy* **36**, 4352-4355 (2008). <https://doi.org/10.1016/j.enpol.2008.09.037>
- 7 Winter, M., Barnett, B. & Xu, K. Before Li Ion Batteries. *Chemical Reviews* **118**, 11433-11456 (2018). <https://doi.org/10.1021/acs.chemrev.8b00422>
- 8 Verma, P., Maire, P. & Novák, P. A review of the features and analyses of the solid electrolyte interphase in Li-ion batteries. *Electrochimica Acta* **55**, 6332-6341 (2010). <https://doi.org/10.1016/j.electacta.2010.05.072>
- 9 Balbuena, P. B. & Wang, Y. (Imperial College Press, 2004).
- 10 Meda, U. S., Lal, L., M, S. & Garg, P. Solid Electrolyte Interphase (SEI), a boon or a bane for lithium batteries: A review on the recent advances. *Journal of Energy Storage* **47** (2022). <https://doi.org/10.1016/j.est.2021.103564>
- 11 Winter, M., Barnett, B. & Xu, K. Before Li Ion Batteries. *Chemical Reviews* **118**, 11433-11456 (2018). <https://doi.org/10.1021/acs.chemrev.8b00422>
- 12 Muralidharan, N. *et al.* Next-Generation Cobalt-Free Cathodes – A Prospective Solution to the Battery Industry's Cobalt Problem. *Advanced Energy Materials* **12**, 2103050 (2022). <https://doi.org/10.1002/aenm.202103050>
- 13 Jin An, S. *et al.* The state of understanding of the lithium-ion battery graphite solid electrolyte interphase and its relationship to formation cycling. *Carbon* **105**, 52-76 (2016). <https://doi.org/10.1016>
- 14 Zheng, J. *et al.* 3D visualization of inhomogeneous multi-layered structure and Young's modulus of the solid electrolyte interphase (SEI) on silicon anodes for lithium ion batteries. *Phys. Chem. Chem. Phys.* **16**, 13229-13238 (2014). <https://doi.org/10.1039/c4cp01968g>
- 15 Liu, W., Liu, P. & Mitlin, D. Review of Emerging Concepts in SEI Analysis and Artificial SEI Membranes for Lithium, Sodium, and Potassium Metal Battery Anodes. *Advanced Energy Materials* **10**, 2002297 (2020). <https://doi.org/10.1002/aenm.202002297>
- 16 Wang, A., Kadam, S., Li, H., Shi, S. & Qi, Y. Review on modeling of the anode solid electrolyte interphase (SEI) for lithium-ion batteries. *npj Computational Materials* **4** (2018). <https://doi.org/10.1038/s41524-018-0064-0>
- 17 KnowItAll. (ed Inc. John Wiley & Sons) (2023).

- 18 (ed S.T. Japan Inc) (2023).
- 19 Weber, G. *et al.* Investigation of hydrolysis of lithium oxide by thermogravimetry, calorimetry and in situ FTIR spectroscopy. *Journal of Thermal Analysis and Calorimetry* **132**, 1055-1064 (2018). <https://doi.org/10.1007/s10973-017-6943-7>
- 20 Bai, W.-L. *et al.* Phosphazene-derived stable and robust artificial SEI for protecting lithium anodes of Li-O<sub>2</sub> batteries. *Chemical Communications* **56**, 12566-12569 (2020). <https://doi.org/10.1039/d0cc05303a>
- 21 Schellenberger, M., Golnak, R., Quevedo Garzon, W. G., Risse, S. & Seidel, R. Accessing the solid electrolyte interphase on silicon anodes for lithium-ion batteries *in-situ* through transmission soft x-ray absorption spectroscopy. *Materials Today Advances* **14** (2022).
- 22 Ota, H., Sakata, Y., Inoue, A. & Yamaguchi, S. Analysis of Vinylene Carbonate Derived SEI Layers on Graphite Anode. *Journal of The Electrochemical Society* **151**, A1659 (2004). <https://doi.org/10.1149/1.1785795>
- 23 Beyer, H. *et al.* Antimony Doped Tin Oxide–Synthesis, Characterization and Application as Cathode Material in Li-O<sub>2</sub> Cells: Implications on the Prospect of Carbon-Free Cathodes for Rechargeable Lithium-Air Batteries. *Journal of The Electrochemical Society* **164**, A1026-A1036 (2017). <https://doi.org/10.1149/2.0441706jes>
- 24 Qiao, Y. *et al.* Li-CO<sub>2</sub> Electrochemistry: A New Strategy for CO<sub>2</sub> Fixation and Energy Storage. *Joule* **1**, 359-370 (2017). <https://doi.org/10.1016/j.joule.2017.07.001>
- 25 Ong, A. C. W., Shamsuri, N. A., Zaine, S. N. A., Panuh, D. & Shukur, M. F. Nanocomposite polymer electrolytes comprising starch-lithium acetate and titania for all-solid-state supercapacitor. *Ionics* **27**, 853-865 (2021). <https://doi.org/10.1007/s11581-020-03856-3>
- 26 Ross, P. Studies of Interfacial Chemistry in Lithium and Li-Ion Battery Systems Using Infrared Spectroscopy. *ECS Transactions* **1**, 161-170 (2006). <https://doi.org/10.1149/1.2209366>
- 27 Sánchez-Carrera, R. S. & Kozinsky, B. Computational Raman spectroscopy of organometallic reaction products in lithium and sodium-based battery systems. *Phys. Chem. Chem. Phys.* **16**, 24549-24558 (2014). <https://doi.org/10.1039/c4cp03998j>
- 28 Ananthanarayanan, V. Raman spectra of single crystals of zinc and lithium acetates dihydrates. *Proceedings of the Indian Academy of Sciences* **56** (1962).
- 29 Martínez Casado, F. J. *et al.* Anhydrous Lithium Acetate Polymorphs and Its Hydrates: Three-Dimensional Coordination Polymers. *Crystal Growth & Design* **11**, 1021-1032 (2011). <https://doi.org/10.1021/cg1010133>
- 30 Cadene, M. Modes normaux de vibrations du monocristal d'acétate de lithium dihydrate. *Journal of Molecular Structure* **2**, 193-208 (1968).
- 31 Heiskanen, K. S., Kim, J. & Lucht, B. L. Generation and Evolution of the Solid Electrolyte Interphase of Lithium-Ion Batteries. *Joule* **3**, 2322-2333 (2019). <https://doi.org/doi.org/10.1016/j.joule.2019.08.018>
- 32 Srout, M., Carboni, M., Gonzalez, J.-A. & Trabesinger, S. Insights into the importance of native passivation layer and interface reactivity of metallic lithium by electrochemical impedance spectroscopy. *Small* **19** (2022).
- 33 Parimalam, B. S., Macintosh, A. D., Kadam, R. & Lucht, B. L. Decomposition Reactions of Anode Solid Electrolyte Interphase (SEI) Components with LiPF<sub>6</sub>. *The Journal of Physical Chemistry C* **121**, 22733-22738 (2017). <https://doi.org/10.1021/acs.jpcc.7b08433>
- 34 Stober, H. C. in *Analytical Profiles of Drug Substances* Vol. 15 (ed Klaus Florey) 367-391 (Academic Press, 1986).
- 35 Özer, S., Şenel, B. & Yazan, Y. Preparation and in vitro evaluation of in situ gelling system containing lithium carbonate for parenteral administration. *Polymer Bulletin* **77**, 599-622 (2020). <https://doi.org/10.1007/s00289-019-02764-5>

- 36 Pasierb, P., Komornicki, S., Rokita, M. & Rękas, M. Structural properties of  $\text{Li}_2\text{CO}_3$ – $\text{BaCO}_3$  system derived from IR and Raman spectroscopy. *Journal of Molecular Structure* **596**, 151-156 (2001). [https://doi.org/10.1016/S0022-2860\(01\)00703-7](https://doi.org/10.1016/S0022-2860(01)00703-7)
- 37 Koura, N. *et al.* Alkali carbonates: Raman spectroscopy, ab initio calculations, and structure. *Journal of Molecular Structure* **382**, 163-169 (1996). [https://doi.org/10.1016/0022-2860\(96\)09314-3](https://doi.org/10.1016/0022-2860(96)09314-3)
- 38 Hase, Y. & Yoshida, I. V. P. Low frequency bands of  $\text{Li}_2\text{CO}_3$  crystal. *Spectrochimica Acta Part A: Molecular Spectroscopy* **35**, 379 (1979). [https://doi.org/10.1016/0584-8539\(79\)80196-8](https://doi.org/10.1016/0584-8539(79)80196-8)
- 39 Jones, W. B., Darvin, J. R., O'Rourke, P. E. & Fessler, K. A. S. Isotopic signatures of lithium carbonate and lithium hydroxide monohydrate measured using Raman spectroscopy. *Applied Spectroscopy* **77**, 151-159 (2023).
- 40 Brooker, M. H. & Bates, J. B. Raman and Infrared Spectral Studies of Anhydrous  $\text{Li}_2\text{CO}_3$  and  $\text{Na}_2\text{CO}_3$ . *The Journal of Chemical Physics* **54**, 4788-4796 (1971). <https://doi.org/10.1063/1.1674754>
- 41 Brooker, M. H. & Wang, J. Raman and infrared studies of lithium and cesium carbonates. *Spectrochimica Acta* **48A**, 999-1008 (1992).
- 42 Taborga, P., Brito, I. & Graber, T. Effect of Additives on Size and Shape of Lithium Carbonate Crystals. *Journal of Crystal Growth* **460** (2016). <https://doi.org/10.1016/j.jcrysgro.2016.12.001>
- 43 Gao, W. *et al.* Lithium Carbonate Recovery from Cathode Scrap of Spent Lithium-Ion Battery: A Closed-Loop Process. *Environmental Science & Technology* **51**, 1662-1669 (2017). <https://doi.org/10.1021/acs.est.6b03320>
- 44 Chen, N., Zhou, E., Duan, D.-P. & Yang, X.-M. Mechanochemistry synthesis of high purity lithium carbonate. *Korean Journal of Chemical Engineering* **34**, 2748-2755 (2017). <https://doi.org/10.1007/s11814-017-0172-4>
- 45 Nie, M. *et al.* Lithium Ion Battery Graphite Solid Electrolyte Interphase Revealed by Microscopy and Spectroscopy. *The Journal of Physical Chemistry C* **117**, 1257-1267 (2013). <https://doi.org/10.1021/jp3118055>
- 46 Widulle, F. *et al.* Isotope effects in elemental semiconductors: a Raman study of silicon. *Solid State Communications* **118**, 1-22 (2001).
- 47 Wada, S., Onaka, T., Yamamura, I., Murata, Y. & Tokunaga, A. T.  $^{13}\text{C}$  isotope effects on infrared bands of quenched carbonaceous composite (QCC). *Astronomy & Astrophysics* **407**, 551-562 (2003). <https://doi.org/10.1051/0004-6361:20030881>
- 48 Rikka, V. R. *et al.* In Situ/ex Situ Investigations on the Formation of the Mosaic Solid Electrolyte Interface Layer on Graphite Anode for Lithium-Ion Batteries. *The Journal of Physical Chemistry C* **122**, 28717-28726 (2018). <https://doi.org/10.1021/acs.jpcc.8b09210>
- 49 Abramowitz, S., Acquista, N. & Levin, I. W. Infrared Matrix Spectra of Lithium Fluoride. *J Res Natl Bur Stand A Phys Chem* **72a**, 487-493 (1968). <https://doi.org/10.6028/jres.072A.041>
- 50 Sarraf-Mamoory, R., Nadery, S. & Riahi-Noori, N. The effect of Precipitation Parameters on preparation of lithium fluoride (LiF) nano-powder. *Chemical Engineering Communications* **194**, 1022-1028 (2007). <https://doi.org/10.1080/00986440701244309>
- 51 Zhang, L., Zhang, K., Shi, Z. & Zhang, S. LiF as an Artificial SEI Layer to Enhance the High-Temperature Cycle Performance of  $\text{Li}_4\text{Ti}_5\text{O}_{12}$ . *Langmuir* **33**, 11164-11169 (2017). <https://doi.org/10.1021/acs.langmuir.7b02031>
- 52 Carturan, S. M. *et al.* Thermal neutron detection by entrapping  $^6\text{LiF}$  nanocrystals in siloxane scintillators. *Journal of Physics: Conference Series* **620**, 012010 (2015). <https://doi.org/10.1088/1742-6596/620/1/012010>

- 53 Paterson, M. S. X-Ray Diffraction by Face-Centered Cubic Crystals with Deformation Faults. *Journal of Applied Physics* **23**, 805-811 (1952). <https://doi.org:10.1063/1.1702312>
- 54 Herrero, C. P., Ramírez, R. & Cardona, M. Isotope effects on the lattice parameter of cubic SiC. *Physical Review B* **79**, 012301 (2009). <https://doi.org:10.1103/PhysRevB.79.012301>
- 55 Tyutyunnik, V. I. & Tyutyunnik, O. I. Phonon Structure of Raman Scattering Spectra of LiH Crystals. *physica status solidi (b)* **162**, 597-604 (1990). <https://doi.org:https://doi.org/10.1002/pssb.2221620233>
- 56 Weber, G. *et al.* New insight on the lithium hydride–water vapor reaction system. *International Journal of Hydrogen Energy* **43**, 22557-22567 (2018). <https://doi.org:https://doi.org/10.1016/j.ijhydene.2018.10.089>
- 57 Carturan, S. M. *et al.* Siloxane-Based Nanocomposites Containing <sup>6</sup>LiF Nanocrystals for Thermal Neutrons Detection. *Acta Physica Polonica A* **134**, 405-408 (2018).
- 58 Zachman, M. J., Tu, Z., Choudhury, S., Archer, L. A. & Kourkoutis, L. F. Cryo-STEM mapping of solid–liquid interfaces and dendrites in lithium-metal batteries. *Nature* **560**, 345-349 (2018). <https://doi.org:10.1038/s41586-018-0397-3>
- 59 Tan, S. *et al.* Identification of Lithium Hydride and Nanocrystalline Lithium Fluoride in the SEI of Lithium Metal Anodes and the Stabilization of High Ni Layered Structure at Ultra-High Voltage through Cathode Electrolyte Interphase Engineering. *ECS Meeting Abstracts* **MA2022-02**, 129 (2022). <https://doi.org:10.1149/MA2022-022129mtgabs>
- 60 Snider, J. L. *et al.* The influence of LiH and TiH<sub>2</sub> on hydrogen storage in MgB<sub>2</sub> I: Promotion of bulk hydrogenation at reduced temperature. *International Journal of Hydrogen Energy* **47**, 387-402 (2022). <https://doi.org:https://doi.org/10.1016/j.ijhydene.2021.09.169>
- 61 Stowe, A. C. & Smyrl, N. Raman spectroscopy of lithium hydride corrosion: Selection of appropriate excitation wavelength to minimize fluorescence. *Vibrational Spectroscopy* **60**, 133-136 (2012). <https://doi.org:10.1016/j.vibspec.2012.01.018>
- 62 Huang, X., Liu, H., Duan, X., Lan, Z. & Guo, J. Co-Addition of Mg<sub>2</sub>Si and Graphene for Synergistically Improving the Hydrogen Storage Properties of Mg–Li Alloy. *Frontiers in Chemistry* **9** (2021). <https://doi.org:10.3389/fchem.2021.775537>
- 63 Yang, L., Ravdel, B. & Lucht, B. L. Electrolyte Reactions with the Surface of High Voltage LiNi<sub>0.5</sub>Mn<sub>1.5</sub>O<sub>4</sub> Cathodes for Lithium-Ion Batteries. *Electrochemical and Solid-State Letters* **13**, A95 (2010). <https://doi.org:10.1149/1.3428515>
- 64 Pekarek, R. T. *et al.* Intrinsic chemical reactivity of solid-electrolyte interphase components in silicon–lithium alloy anode batteries probed by FTIR spectroscopy. *Journal of Materials Chemistry A* **8**, 7897-7906 (2020). <https://doi.org:10.1039/c9ta13535a>
- 65 Kock, L. D., Lekgoathi, M. D. S., Crouse, P. L. & Vilakazi, B. M. Solid state vibrational spectroscopy of anhydrous lithium hexafluorophosphate (LiPF<sub>6</sub>). *Journal of Molecular Structure* **1026**, 145-149 (2012). <https://doi.org:10.1016/j.molstruc.2012.05.053>
- 66 Cabo-Fernandez, L. *et al.* Kerr gated Raman spectroscopy of LiPF<sub>6</sub> salt and LiPF<sub>6</sub>-based organic carbonate electrolyte for Li-ion batteries. *Physical Chemistry Chemical Physics* **21**, 23833-23842 (2019). <https://doi.org:10.1039/c9cp02430a>
- 67 Lekgoathi, M. D. S. & Kock, L. D. Effect of short and long range order on crystal structure interpretation: Raman and powder X-ray diffraction of LiPF<sub>6</sub>. *Spectrochimica Acta Part A: Molecular and Biomolecular Spectroscopy* **153**, 651-654 (2016). <https://doi.org:https://doi.org/10.1016/j.saa.2015.09.025>
- 68 Han, S.-D. *et al.* Solvate Structures and Computational/Spectroscopic Characterization of LiPF<sub>6</sub> Electrolytes. *The Journal of Physical Chemistry C* **119**, 8492-8500 (2015). <https://doi.org:10.1021/acs.jpcc.5b00826>

- 69 Liu, J.-w. *et al.* Preparation and characterization of lithium hexafluorophosphate for lithium-ion battery electrolyte. *Transactions of Nonferrous Metals Society of China* **20**, 344-348 (2010). [https://doi.org/10.1016/S1003-6326\(09\)60144-8](https://doi.org/10.1016/S1003-6326(09)60144-8)
- 70 Masoud, E. M., Hassan, M. E., Wahdaan, S. E., Elsayed, S. R. & Elsayed, S. A. Gel P (VdF/HFP) / PVAc / lithium hexafluorophosphate composite electrolyte containing nano ZnO filler for lithium ion batteries application: Effect of nano filler concentration on structure, thermal stability and transport properties. *Polymer Testing* **56**, 277-286 (2016). <https://doi.org/10.1016/j.polymertesting.2016.10.028>
- 71 Tian, N., Hua, C., Wang, Z. & Chen, L. Reversible reduction of  $\text{Li}_2\text{CO}_3$ . *Journal of Materials Chemistry A* **3**, 14173-14177 (2015). <https://doi.org/10.1039/c5ta02499d>
- 72 Oohira, S., Kakihana, M., Fujii, Y., Nagumo, T. & Okamoto, M. Spectroscopic analysis of lithium hydroxide and carbonate in solid state lithium oxide. *Journal of Nuclear Materials* **133-134**, 201-204 (1985). [https://doi.org/10.1016/0022-3115\(85\)90134-5](https://doi.org/10.1016/0022-3115(85)90134-5)
- 73 Wijaya, O. *et al.* A gamma fluorinated ether as an additive for enhanced oxygen activity in  $\text{Li-O}_2$  batteries. *Journal of Materials Chemistry A* **3**, 19061-19067 (2015). <https://doi.org/10.1039/c5ta03439f>
- 74 Kurasawa, T. & Maroni, V. A. Infrared spectroscopic analysis of  $\text{OH}^-$  and  $\text{OD}^-$  in crystalline  $\text{Li}_2\text{O}$  as a function of chemical treatment. *Journal of Nuclear Materials* **119**, 95-101 (1983). [https://doi.org/10.1016/0022-3115\(83\)90057-0](https://doi.org/10.1016/0022-3115(83)90057-0)
- 75 Tanaka, S., Taniguchi, M., Nakatani, M., Yamaki, D. & Yamawaki, M. In situ observation of surface  $-\text{OH}$  and  $-\text{OD}$  on lithium oxide. *Journal of Nuclear Materials* **218**, 335-338 (1995). [https://doi.org/10.1016/0022-3115\(94\)00678-4](https://doi.org/10.1016/0022-3115(94)00678-4)
- 76 Jones, L. H. The Infrared Spectra and Structure of  $\text{LiOH}$ ,  $\text{LiOH}\cdot\text{H}_2\text{O}$  and the Deuterium Species. Remark on Fundamental Frequency of  $\text{OH}^-$ . *The Journal of Chemical Physics* **22**, 217-219 (1954). <https://doi.org/10.1063/1.1740033>
- 77 Osaka, T. & Shindo, I. Infrared reflectivity and Raman scattering of lithium oxide single crystals. *Solid State Communications* **51**, 421-424 (1984).
- 78 Sifuentes, A., Stowe, A. C. & Smyrl, N. Determination of the role of  $\text{Li}_2\text{O}$  on the corrosion of lithium hydride. *Journal of Alloys and Compounds* **580**, S271-S273 (2013). <https://doi.org/10.1016/j.jallcom.2013.02.046>
- 79 Gittleson, F. S., Ryu, W.-H. & Taylor, A. D. Operando Observation of the Gold-Electrolyte Interface in  $\text{Li-O}_2$  Batteries. *ACS Applied Materials & Interfaces* **6**, 19017-19025 (2014). <https://doi.org/10.1021/am504900k>
- 80 Miyaoka, H. *et al.* Kinetic Modification on Hydrogen Desorption of Lithium Hydride and Magnesium Amide System. *Materials (Basel)* **8**, 3896-3909 (2015). <https://doi.org/10.3390/ma8073896>
- 81 Furukawa, T., Hirakawa, Y., Kondo, H. & Kanemura, T. Dissolution behavior of lithium compounds in ethanol. *Nuclear Materials and Energy* **9** (2016). <https://doi.org/10.1016/j.nme.2016.05.005>
- 82 Jain, A. *et al.* Commentary: The Materials Project: A materials genome approach to accelerating materials innovation. *APL Materials* **1**, 011002 (2013). <https://doi.org/10.1063/1.4812323>
- 83 Schnabel, M. *et al.* Stable SEI Formation on Al-Si-Mn Metallic Glass Li-Ion Anode. *Journal of The Electrochemical Society* **168**, 100521 (2021). <https://doi.org/10.1149/1945-7111/ac2d3f>
- 84 Rui, K., Wen, Z., Lu, Y., Jin, J. & Shen, C. One-Step Solvothermal Synthesis of Nanostructured Manganese Fluoride as an Anode for Rechargeable Lithium-Ion Batteries and Insights into the Conversion Mechanism. *Advanced Energy Materials* **5**, 1401716 (2015). <https://doi.org/10.1002/aenm.201401716>

- 85 Zhou, J. *et al.* Dual-Salt Electrolyte Additives Enabled Stable Lithium Metal Anode/Lithium–Manganese-Rich Cathode Batteries. *Advanced Energy and Sustainability Research* **3**, 2100140 (2022). <https://doi.org:10.1002/aesr.202100140>
- 86 Croy, J. R. *et al.* Development of manganese-rich cathodes as alternatives to nickel-rich chemistries. *Journal of Power Sources* **434**, 226706 (2019). <https://doi.org:https://doi.org/10.1016/j.jpowsour.2019.226706>
- 87 Scholz, G. & Stösser, R. Molecular structures, vibrational frequencies and isotropic hyperfine coupling constants FeF<sub>3</sub> and MnF<sub>2</sub>: an initio molecular orbital study. *Journal of Molecular Structure* **488**, 195-206 (1999).
- 88 Stavrou, E., Yao, Y., Goncharov, A. F., Konôpková, Z. & Raptis, C. High-pressure structural study of MnF<sub>2</sub>. *Physical Review B* **93** (2016). <https://doi.org:10.1103/physrevb.93.054101>
- 89 Rui, K. *et al.* High-performance lithium storage in an ultrafine manganese fluoride nanorod anode with enhanced electrochemical activation based on conversion reaction. *Physical Chemistry Chemical Physics* **18**, 3780-3787 (2016). <https://doi.org:10.1039/c5cp07361h>
- 90 Li, X., Lu, J., Peng, G., Jin, L. & Wei, S. Solvothermal synthesis of MnF<sub>2</sub> nanocrystals and the first-principle study of its electronic structure. *Journal of Physics and Chemistry of Solids* **70**, 609-615 (2009). <https://doi.org:https://doi.org/10.1016/j.jpics.2009.01.004>
- 91 Grenier, A. *et al.* Synthesis and optimized formulation for high-capacity manganese fluoride (MnF<sub>2</sub>) electrodes for lithium-ion batteries. *Journal of Fluorine Chemistry* **224**, 45-51 (2019). <https://doi.org:https://doi.org/10.1016/j.jfluchem.2019.05.007>
- 92 Jiao, A.-J., Gao, J.-F., He, Z.-H., Hou, J.-F. & Kong, L.-B. Nickel Fluoride Nanorods as Anode Materials for Li-Ion Hybrid Capacitors. *ACS Applied Nano Materials* **4**, 11601-11610 (2021). <https://doi.org:10.1021/acsanm.1c02140>
- 93 Kim, J., Chae, O. B. & Lucht, B. L. Perspective—Structure and Stability of the Solid Electrolyte Interphase on Silicon Anodes of Lithium-ion Batteries. *Journal of The Electrochemical Society* **168** (2021). <https://doi.org:10.1149/1945-7111/abe984>
- 94 Yoon, M. *et al.* Reactive boride infusion stabilizes Ni-rich cathodes for lithium-ion batteries. *Nature Energy* **6**, 362-371 (2021). <https://doi.org:10.1038/s41560-021-00782-0>
- 95 Tramšek, M. & Žemva, B. Higher Fluorides of Nickel: Synthesis and some Properties of Ni<sub>2</sub>F<sub>5</sub>. *Acta Chimica Slovenica* **49**, 209-220 (2002).
- 96 Ullah, H., Batisse, N., Guerin, K., Rogez, G. & Bonnet, P. Synthesis of NiF<sub>2</sub> and NiF<sub>2</sub>·4H<sub>2</sub>O Nanoparticles by Microemulsion and Their Self-Assembly. *Langmuir* **36**, 8461-8475 (2020). <https://doi.org:10.1021/acs.langmuir.0c00889>
- 97 Lee, D. H., Carroll, K. J., Calvin, S., Jin, S. & Meng, Y. S. Conversion mechanism of nickel fluoride and NiO-doped nickel fluoride in Li ion batteries. *Electrochimica Acta* **59**, 213-221 (2012). <https://doi.org:https://doi.org/10.1016/j.electacta.2011.10.105>
- 98 Ocadiz-Flores, J. A., Capelli, E., Raison, P. E., Konings, R. J. M. & Smith, A. L. Thermodynamic assessment of the LiF-NiF<sub>2</sub>, NaF-NiF<sub>2</sub> and KF-NiF<sub>2</sub> systems. *The Journal of Chemical Thermodynamics* **121**, 17-26 (2018). <https://doi.org:https://doi.org/10.1016/j.jct.2018.01.023>
- 99 Xue, Z., He, D. & Xie, X. Poly(ethylene oxide)-based electrolytes for lithium-ion batteries. *Journal of Materials Chemistry A* **3**, 19218-19253 (2015). <https://doi.org:10.1039/c5ta03471j>
- 100 Assegie, A. A., Cheng, J.-H., Kuo, L.-M., Su, W.-N. & Hwang, B.-J. Polyethylene oxide film coating enhances lithium cycling efficiency of an anode-free lithium-metal battery. *Nanoscale* **10**, 6125-6138 (2018). <https://doi.org:10.1039/c7nr09058g>
- 101 Jin, Y. *et al.* Identifying the Structural Basis for the Increased Stability of the Solid Electrolyte Interphase Formed on Silicon with the Additive Fluoroethylene Carbonate.



- Journal of the American Chemical Society* **139**, 14992-15004 (2017).  
<https://doi.org:10.1021/jacs.7b06834>
- 102 Wardhani, R. A. K., Asri, L., Nasir, M. & Purwasasmita, B. S. Preparation of Chitosan-Polyethylene Oxide-Colocasia esculenta Flour Nanofibers using Electrospinning Method. *Journal of Mechanical Engineering Science and Technology* **3**, 1-7 (2019).  
<https://doi.org:10.17977/um016v3i12019p001>
- 103 Gupta, B., Agarwal, R. & Sarwar Alam, M. Preparation and characterization of polyvinyl alcohol-polyethylene oxide-carboxymethyl cellulose blend membranes. *Journal of Applied Polymer Science* **127**, 1301-1308 (2013). <https://doi.org:10.1002/app.37665>
- 104 Monir, T. S. B. *et al.* pH-Sensitive Hydrogel from Polyethylene Oxide and Acrylic acid by Gamma Radiation. *Journal of Composites Science* **3**, 58 (2019).  
<https://doi.org:10.3390/jcs3020058>
- 105 Roy, A., Dutta, B. & Bhattacharya, S. Ion dynamics in NaBF<sub>4</sub> salt-complexed PVC-PEO blend polymer electrolytes: correlation between average ion hopping length and network structure. *Ionics* **23**, 3389-3399 (2017). <https://doi.org:10.1007/s11581-017-2154-2>
- 106 Xu, Y. *et al.* Preparation and characterization of electrospun PHBV/PEO mats: The role of solvent and PEO component. *Journal of Materials Science* **51**, 5695-5711 (2016).  
<https://doi.org:10.1007/s10853-016-9872-0>
- 107 Tadokoro, H., Chatani, Y., Yoshihara, T., Tahara, S. & Murahashi, S. Structural Studies on Polyethers, [-(CH<sub>2</sub>)<sub>m</sub>-O]<sub>n</sub>. II<sup>1</sup>. Molecular Structure of Polyethylene Oxide. *Die Makromolekulare Chemie* **73**, 109-127 (1964).  
<https://doi.org:10.1002/macp.1964.020730109>
- 108 Jurado, J., Vargas hernandez, C. & Vargas, R. A. Preparation of zinc oxide and polyethylene oxide composite membranes and their phase relationship. *DYNA* **79**, 79-85 (2012).
- 109 Blaszczyk-Lezak, I., Maiz, J., Sacristán, J. & Mijangos, C. Monitoring the Thermal Elimination of Infiltrated Polymer from AAO Templates: An Exhaustive Characterization after Polymer Extraction. *Industrial & Engineering Chemistry Research* **50**, 10883-10888 (2011). <https://doi.org:10.1021/ie200826x>
- 110 Alhusiki-Alghamdi, H. M. & Alghunaim, N. S. Spectroscopic Studies of Nanocomposites Based on PEO/PVDF Blend Loaded by SWCNTs. *Journal of Modern Physics* **06**, 414-424 (2015). <https://doi.org:10.4236/jmp.2015.64045>
- 111 Vanita, V., Waidha, A. I., Yadav, S., Schneider, J. J. & Clemens, O. *Conductivity enhancement within garnet-rich polymer composite electrolytes via the addition of succinonitrile* (American Chemical Society (ACS), 2022).
- 112 Money, B. K. & Hariharan, K. Lithium ion conduction in lithium metaphosphate based systems. *Applied Physics A* **88**, 647-652 (2007). <https://doi.org:10.1007/s00339-007-4020-y>
- 113 Polu, A. R. & Rhee, H.-W. The Effects of LiTDI Salt and POSS-PEG (n = 4) Hybrid Nanoparticles on Crystallinity and Ionic Conductivity of PEO Based Solid Polymer Electrolytes. *Science of Advanced Materials* **8**, 931-940 (2016).  
<https://doi.org:10.1166/sam.2016.2657>
- 114 Matsui, Y., Kubota, T., Tadokoro, H. & Yoshihara, T. Raman Spectra of Polyethers. *Journal of Polymer Science: Part A* **3**, 2275-2288 (1965).
- 115 Ratna, D., Divekar, S., Samui, A. B., Chakraborty, B. C. & Banthia, A. K. Poly(ethylene oxide)/clay nanocomposite: Thermomechanical properties and morphology. *Polymer* **47**, 4068-4074 (2006).  
<https://doi.org:https://doi.org/10.1016/j.polymer.2006.02.040>
- 116 Telfah, A. *et al.* HR MAS NMR, dielectric impedence and XRD characterization of polyethylene oxide films for structural phase transitions. *Physica B: Condensed Matter* **646**, 414353 (2022). <https://doi.org:https://doi.org/10.1016/j.physb.2022.414353>

